Electronic Supplementary Material (ESI) for Journal of Materials Chemistry A.
This journal is © The Royal Society of Chemistry 2020

Supporting Information

Polymer Dielectrics Exhibiting Anomalously Improved Dielectric Constant and Simultaneously Achieved High Energy Density and Efficiency Enabled by CdSe/$Cd_{1-x}Zn_xS$ Quantum Dots

Li Li,[a] Jingsai Cheng,[b] Yunyun Cheng,[a] Ting Han,[a] Xiao Liang,[a] Yan Zhao,[b] Guanghui Zhao[b] and Lijie Dong*[a]*

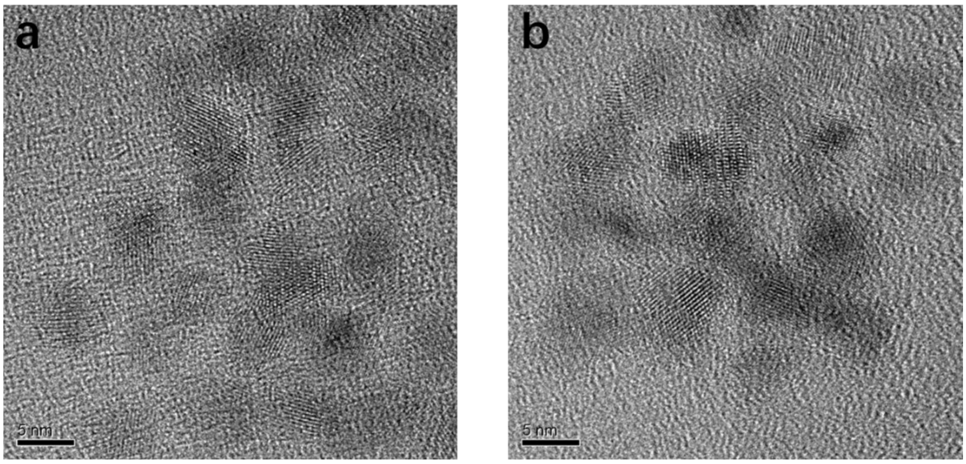

Fig. S1. HRTEM images of a) QDs–OA and b) QDs–M. Scale bar is 5 nm.

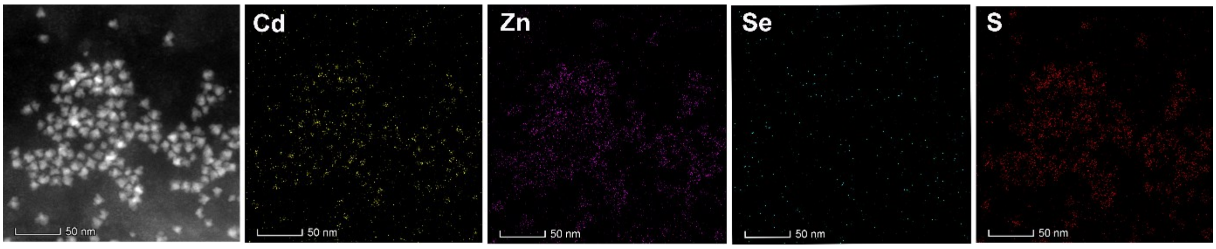

Fig. S2. HAADF image of QDs and EDS mapping of Cd, Zn, Se and S.

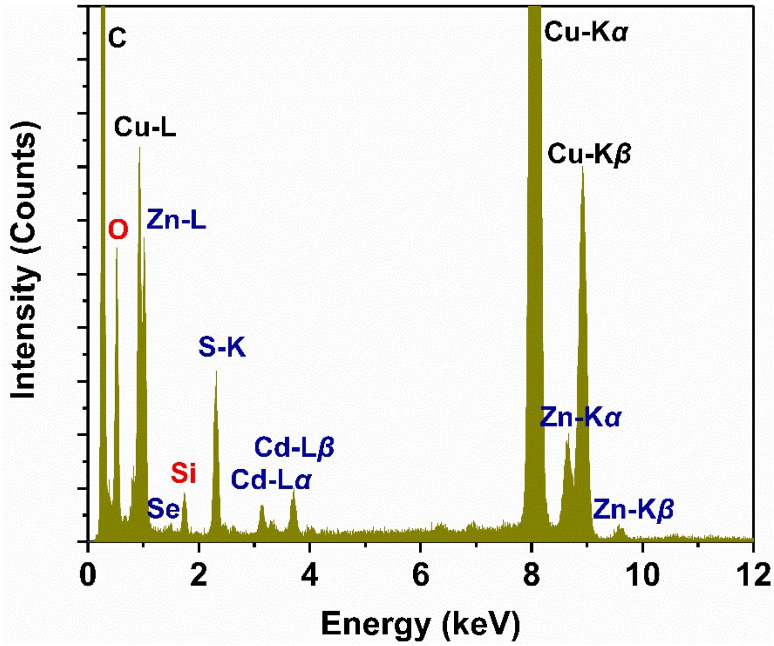

Fig. S3. EDS spectrum of QDs. It clearly shows the characteristic peaks of Cd, Zn, Se and elements. It also proves the existence of perfuorinated group due to observation of O and Si. The intensity ratio of Zn to Cd is about 8:2.

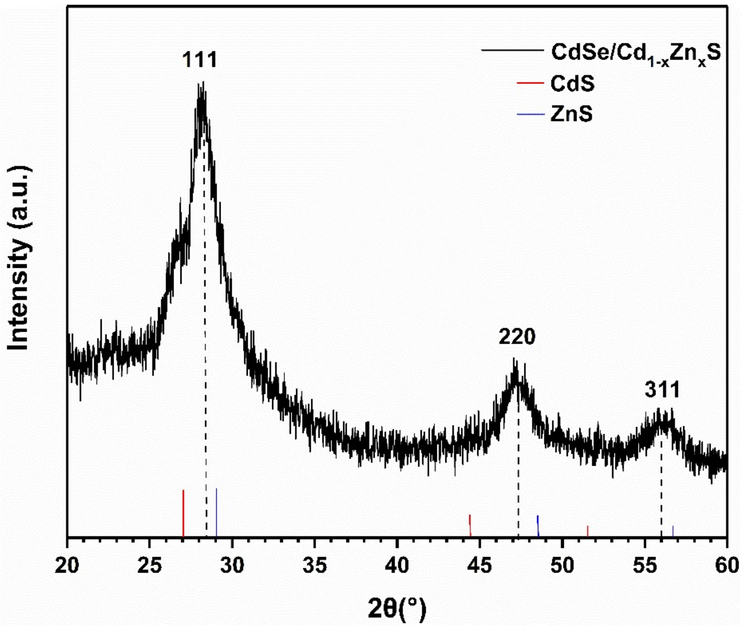

Fig. S4. XRD pattern of QDs. According to Bragg equation:[1]

$$\lambda = 2d\sin\theta \qquad (1)$$

where λ is the wavelength of X-ray (Cu Kα), 0.154056 nm, d is the interplanar spacing and θ is the diffraction angel, we can get d = 0.321 nm for the (111) plane, which is in agreement of HRTEM result. Then, we can obtain the lattice constant based on the lattice constant–interplanar spacing relationship of cubic lattice:[2]

$$a = d_{hkl}\sqrt{(h^2 + k^2 + l^2)} \qquad (2)$$

where a is lattice constant, d_{hkl} is the interplanar spacing for (hkl) plane and h, k, l are Miller indices. So we can determine the value of x of the alloyed $Cd_{1-x}Zn_xS$ shell of QDs from Vegard's law:[3]

$$a = (1 - x)a_{CdS} + xa_{ZnS} \qquad (3)$$

where a_{CdS} and a_{ZnS} are the lattice constant for CdS and ZnS, respectively, both of which share a similar cubic symmetry. The result is x = 0.12 and the composition of QDs is $CdSe/Cd_{0.12}Zn_{0.88}S$. The Zn/Cd ratio is about 7.33, in accordance with EDS result. This is interpreted that one Cd atom replaces a position of Zn atom in ZnS crystal and is shared by two unit cells of ZnS. Based on this result, the crystal structure of QDs is pictured in Fig. S5b.

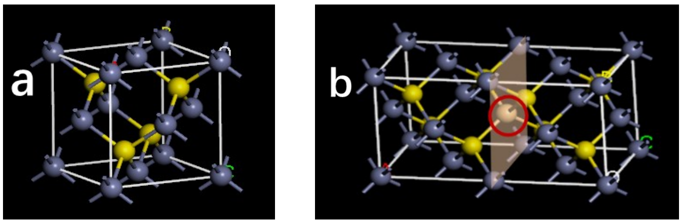

Fig. S5. Unit cells of a) ZnS and b) $Cd_{0.12}Zn_{0.88}S$. The spheres colored by purple, yellow and grey represent Zn, S and Cd, respectively.

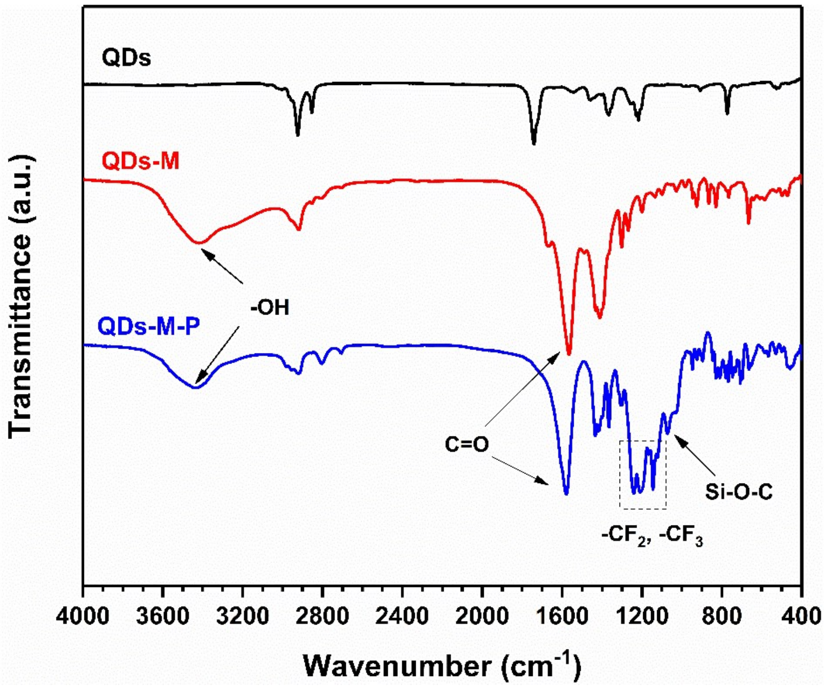

Fig. S6. FTIR spectra of QDs (black), QDs–M (red) and QDs–M–P (blue). In the spectra of QDs–M and QDs–M–P, the peaks at 3420 cm^{-1} are assigned to vibration of –OH from MPA; but the one for QDs–M–P is smaller than that of QDs–M, indicating –OH is consumed by the grafting of POTS. Compared to QDs–M, new peaks at 1120 to 350 cm^{-1} are shown in the spectra of QDs–M–P, which are attributed to vibration of –CF_2 and –CF_3. Also, a peak at 1066 cm^{-1} is found and assigned to Si–O–C. The peaks at around 1580 cm^{-1} correspond to absorption of C=O. The peak shift occurred here signifies a changed electron cloud distribution due to the grafting of –$OSiC_2H_4(CF_2)_6F$ to C=O replacing –OH. These results proves that the fluorinated groups have been bonded with MPA through forming C–O–Si bond.

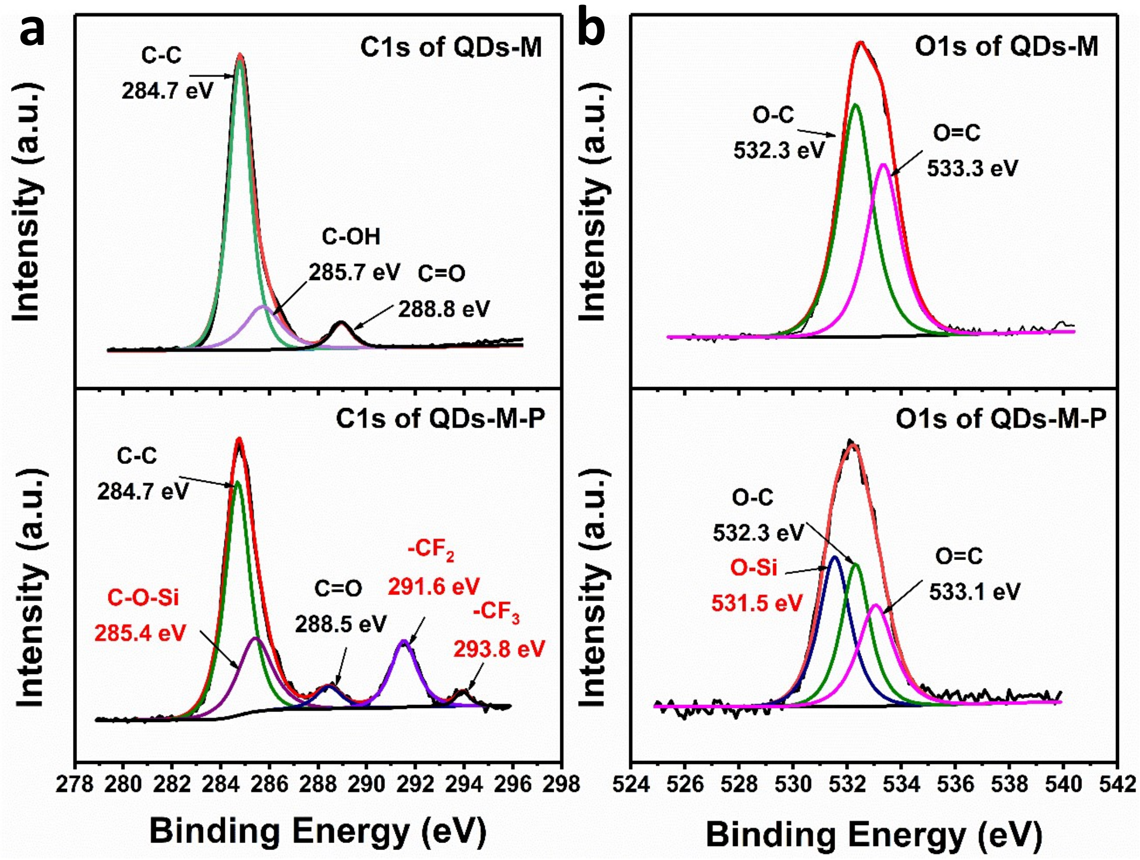

Fig. S7. High resolution XPS spectra of a) C1s and b) O1s of QDs–M (top) and QDs–M–P (down).

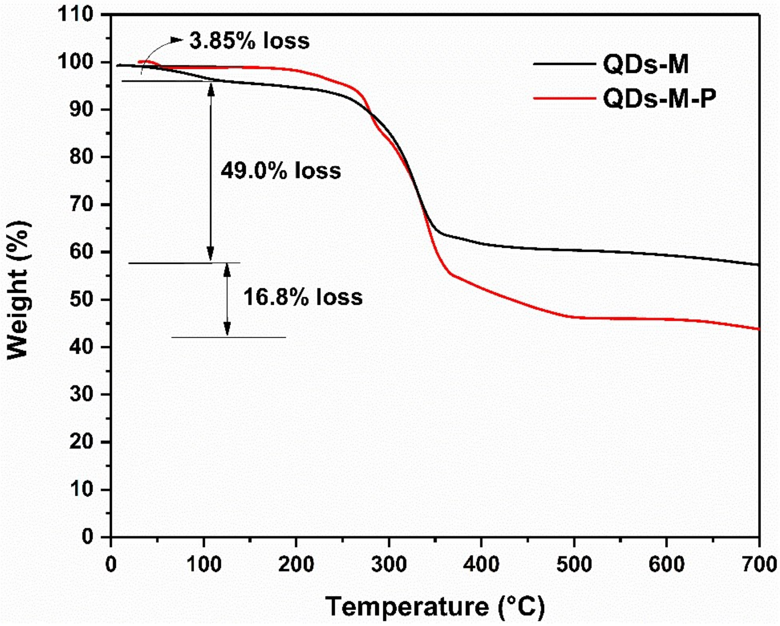

Fig. S8. TGA curves of QDs–M (black) and QDs–M–P (red). For QDs–M, the major weight loss is 49.0% and occurs at 150–350 °C, corresponding to the loss of MPA. For QDs–M–P, there are two major weight loss at 150–350 °C and 350–500 °C, the former is for MPA and the latter is due to loss of POTS, which has high temperature stability, in agreement with literatures. Note that the real weight ratio of POTS cannot be obtained from simply subtracting the total loss of MPA and POTS in QDs–M–P from the loss of MPA in the QDs–M, *i.e.*, 16.8%, since there is a small loss of 3.85% below 100 ℃ in QDs–M attributed to the absorbed water; while no loss is observed here in QDs–M–P due to the hydrophobic nature of POTS. Therefore, the loss for water must be subtracted first. After that, the real weight ratio of MPA (ω_m) and POTS (ω_p) is determined to be 69.65% and 18.69%, respectively. And the rest is for intrinsic QDs (ω_{QD}, 30.35%). Based on these results, we can approximately obtain the average amount and surface density of POTS on each QD following these equations:

$$m_{QD} = \frac{4\pi\rho_{QD}\left(\frac{D}{2}\right)^3}{3} \qquad (4)$$

$$m_p = \frac{m_{QD}}{\omega_{QD}}\omega_p \qquad (5)$$

$$N_p = \frac{m_p}{M_p}N_A \qquad (6)$$

$$\rho_p = \frac{N_p}{\pi(\frac{D}{2})^2} \qquad (7)$$

where m_{QD}, m_p are the mass of single QD and POTS grafted on the QD, respectively; ρ_{QD} is the density of QDs, 4.34 g cm^{-3}; D is the diameter of QDs, 6.8 nm; N_p, M_p, N_A are the average amount of POTS on each QD, molar mass of POTS, 510 g mol^{-1} and Avogadro constant, 6.02×10^{23}, respectively. And ρ_p is the surface density of POTS on QD. The results show $N_p\approx149.8$ and $\rho_p\approx1.03$ nm^{-2}.

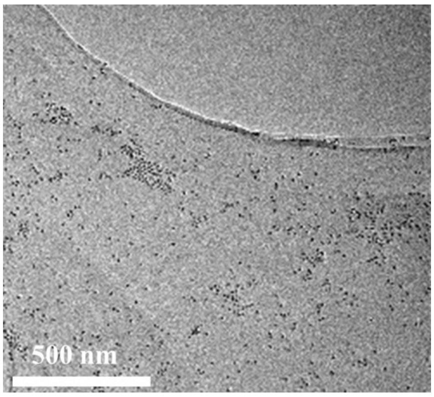

Fig. S9. Typical TEM image of P(VDF-HFP)/QDs–M–P nanocomposite.

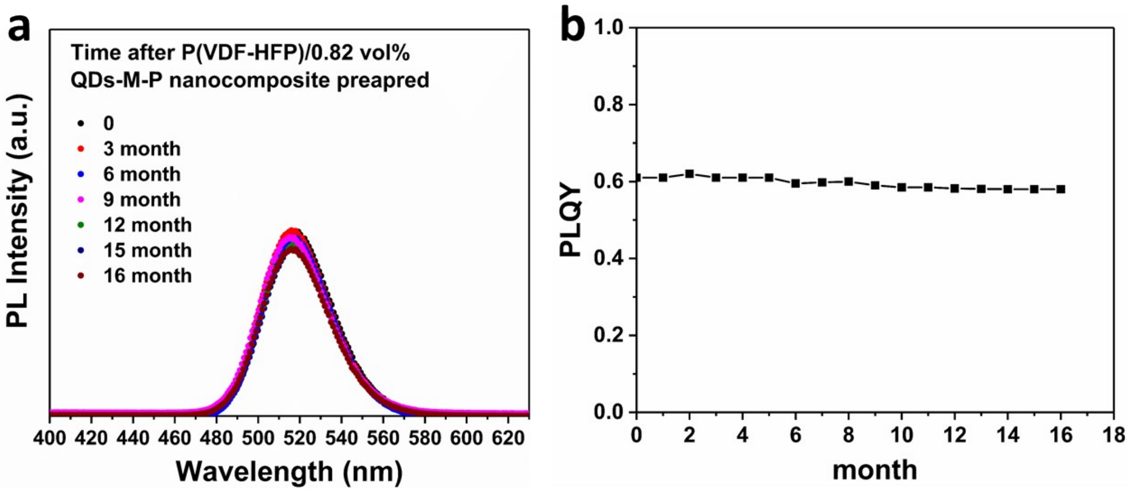

Fig. S10. a) PL spectra and b) PLQY of P(VDF-HFP)/0.82 vol% QDs–M–P nanocomposite measured under different time from when the nanocomposite was prepared to 16 months later under ambient air conditions.

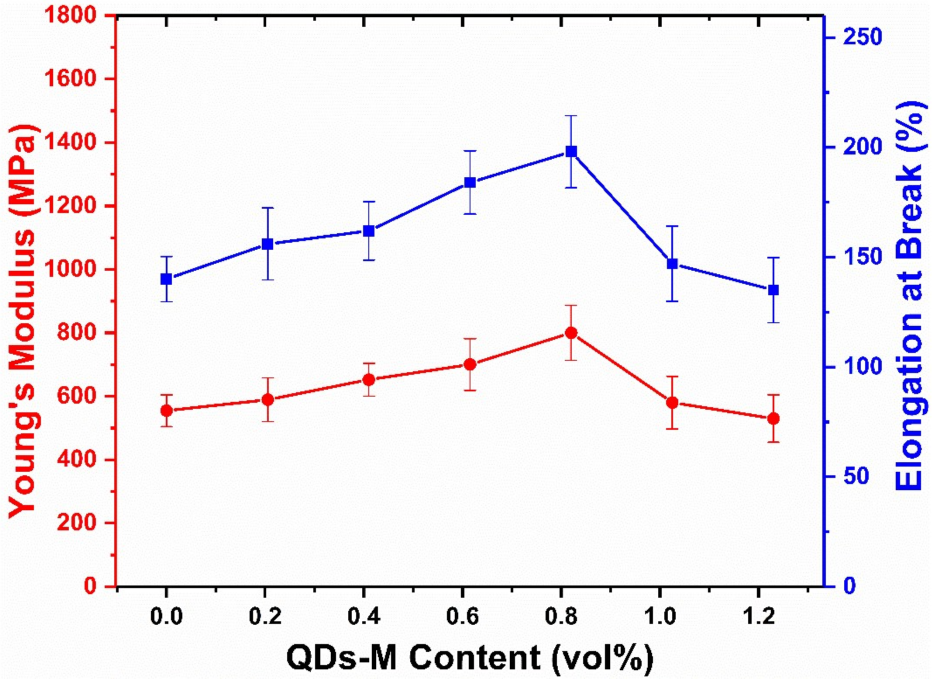

Fig. S11. Young's modulus (red) and elongation at break (blue) of pure P(VDF-HFP) and a series of P(VDF-HFP)/QDs–M nanocomposites as a function of QDs–M content.

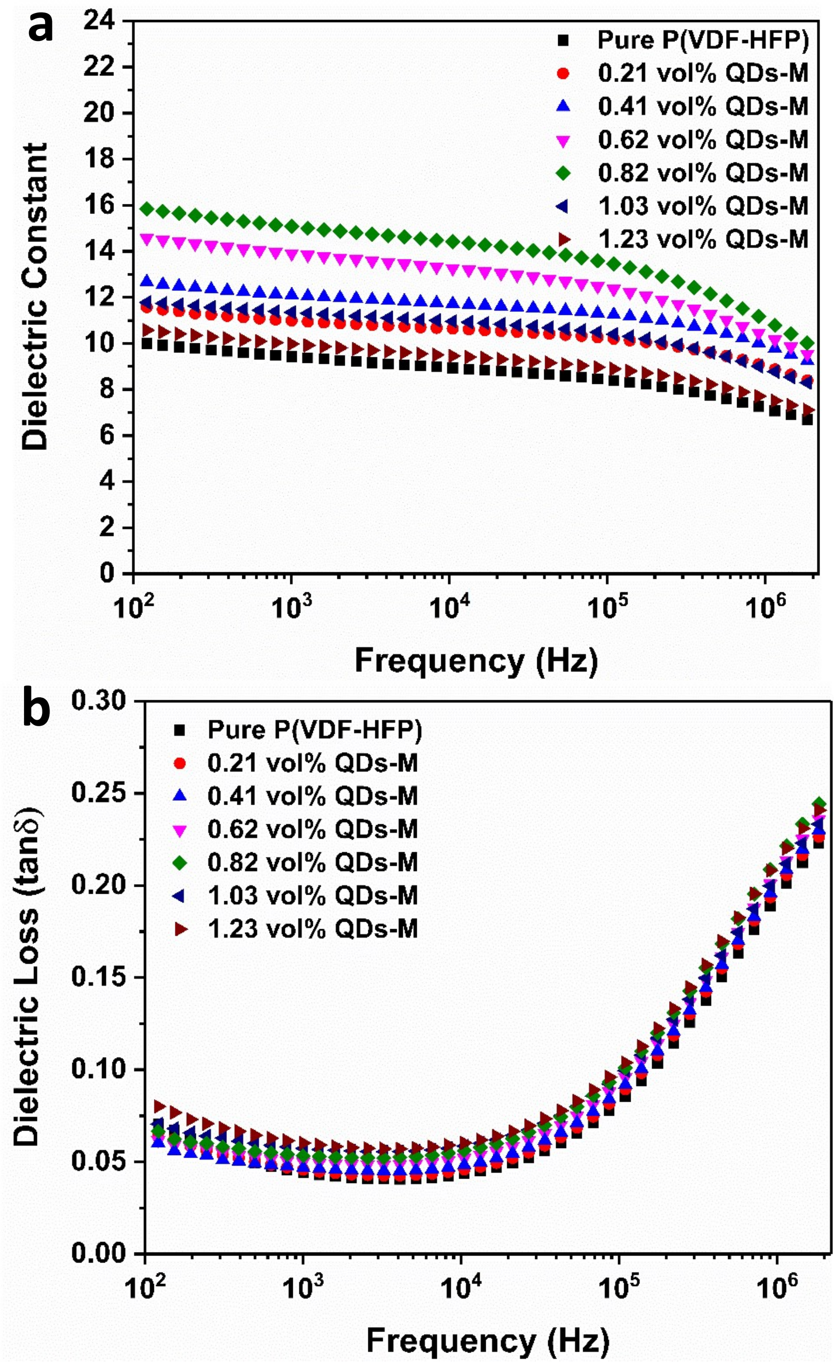

Fig. S12. Frequency–dependent a) dielectric constant and b) dielectric loss of pure P(VDF-HFP) and a series of P(VDF-HFP)/QDs–M nanocomposites with a frequency range from 20 Hz to 2 MHz at room temperature.

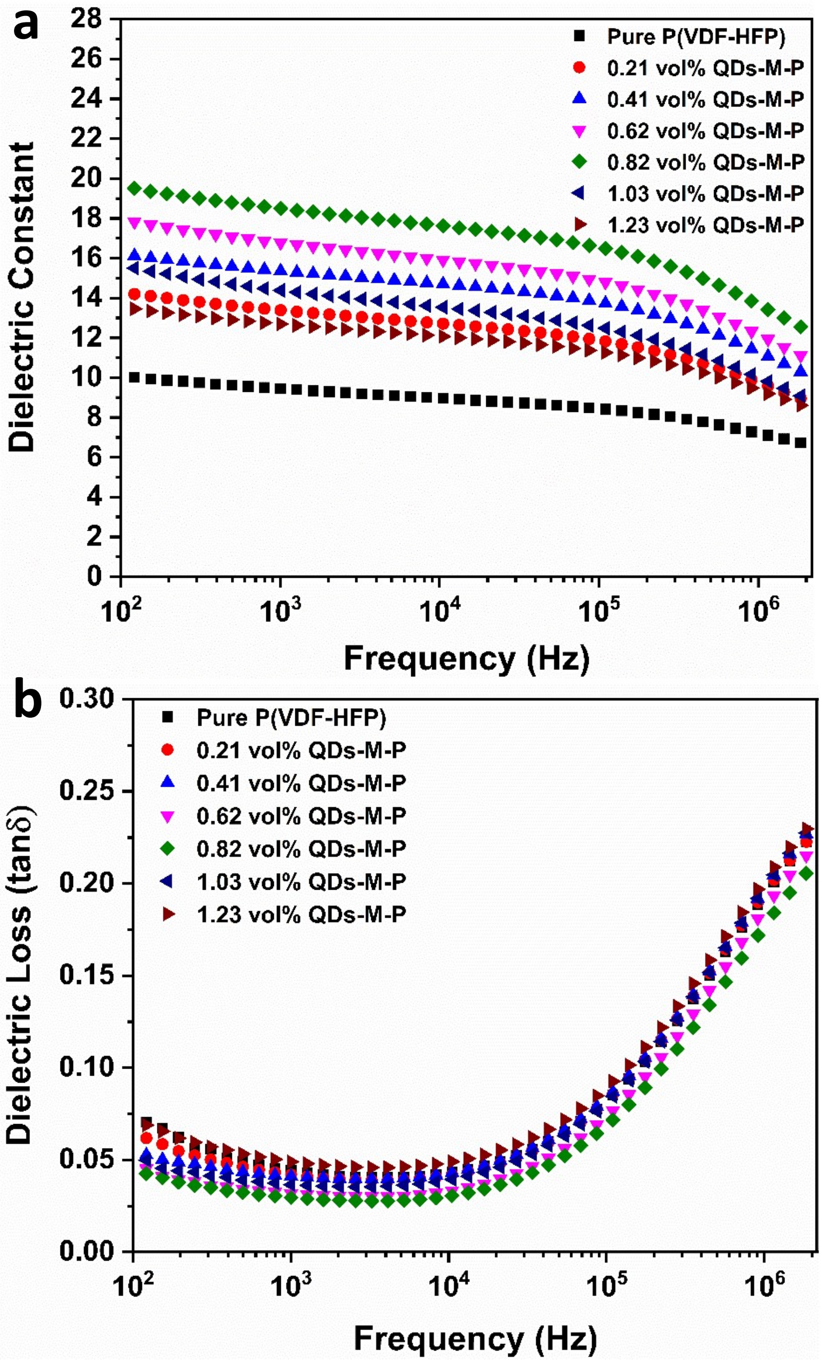

Fig. S13. Frequency-dependent a) dielectric constant and b) dielectric loss of pure P(VDF-HFP) and a series of P(VDF-HFP)/QDs–M–P nanocomposites with a frequency range from 20 Hz to 2 MHz at room temperature.

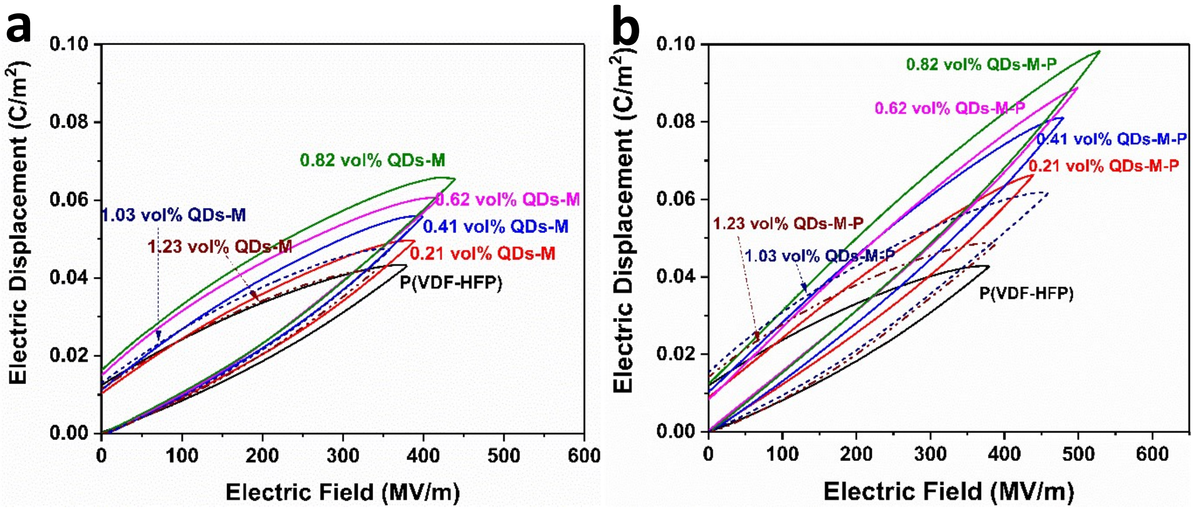

Fig. S14. P–E loops of pure P(VDF-HFP) and a series of (a) P(VDF-HFP)/QDs–M and (b) P(VDF-HFP)/QDs–M-P nanocomposites under maximum electric fields.

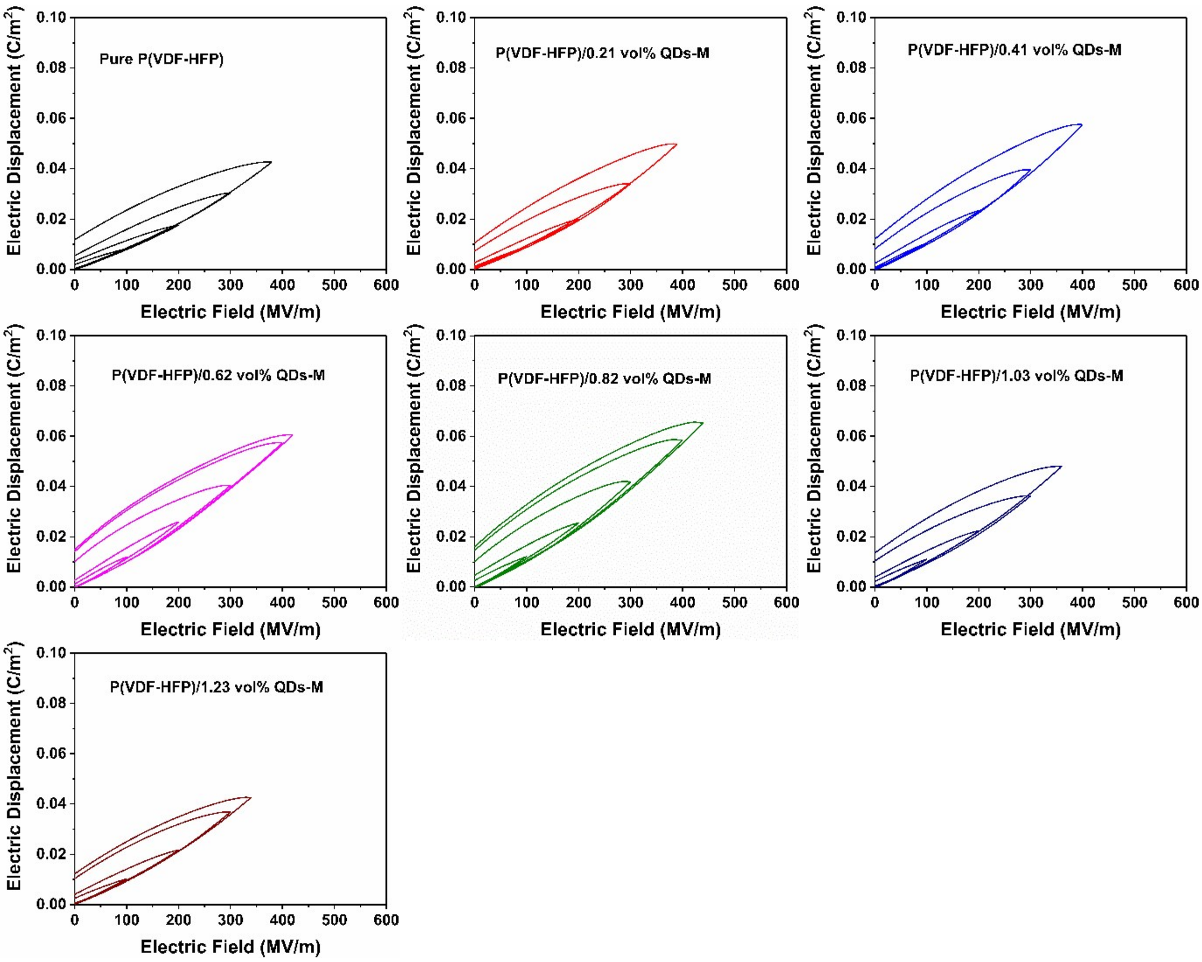

Fig. S15. P–E loops of pure P(VDF-HFP) and a series of P(VDF-HFP)/QDs–M nanocomposites.

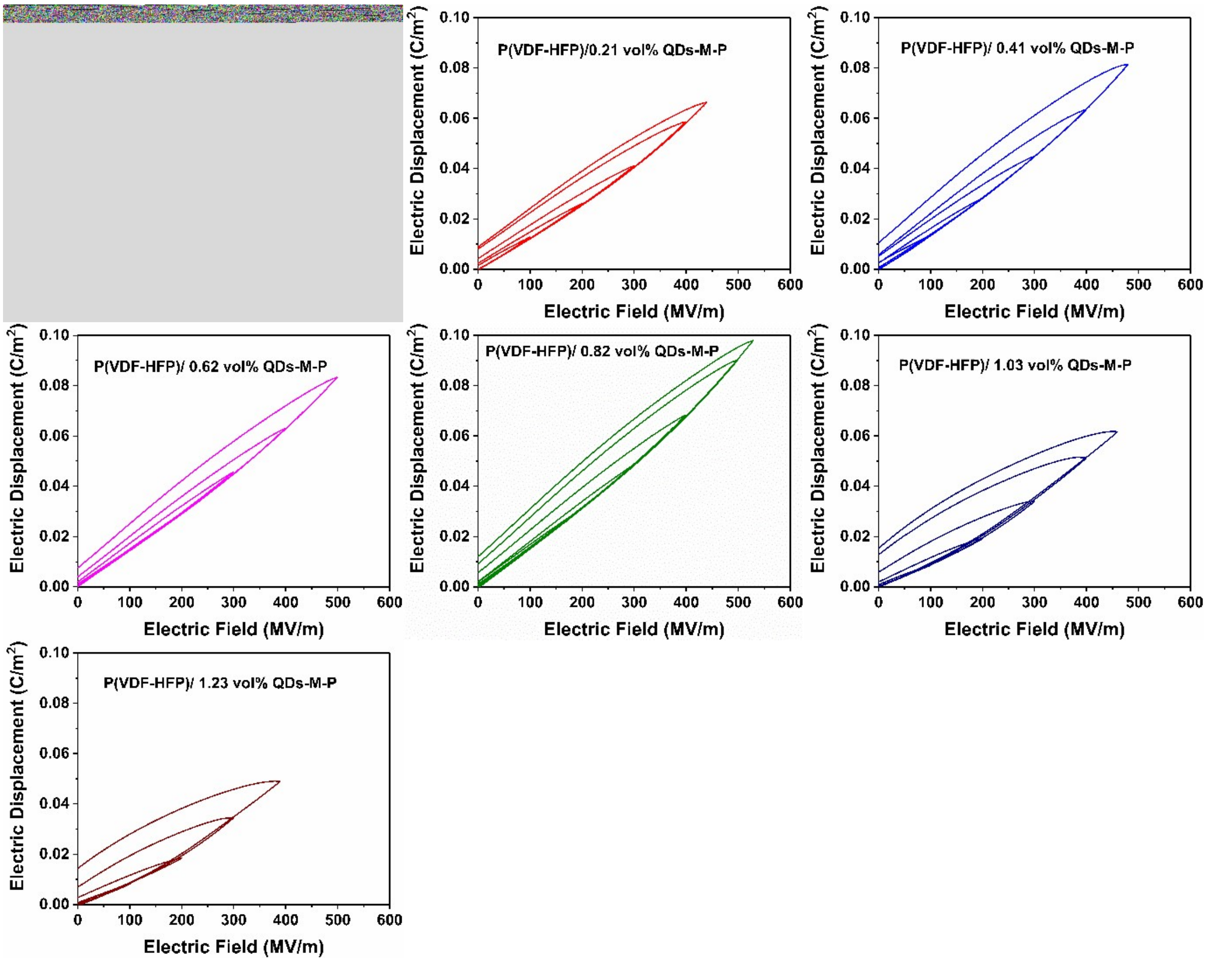

Fig. S16. P–E loops of pure P(VDF-HFP) and a series of P(VDF-HFP)/QDs–M–P nanocomposites.

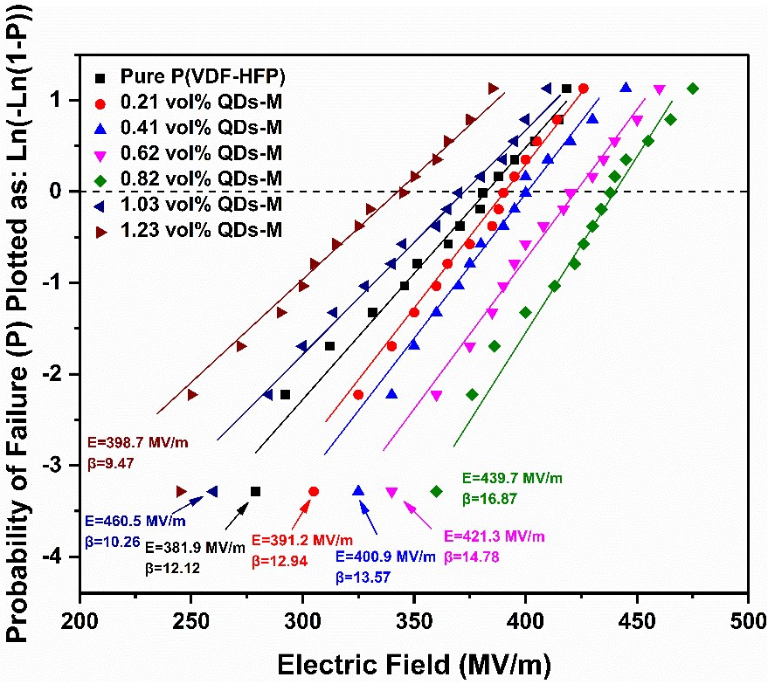

Fig. 17. Weibull plots of pure P(VDF-HFP) and a series of P(VDF-HFP)/QDs–M nanocomposites.

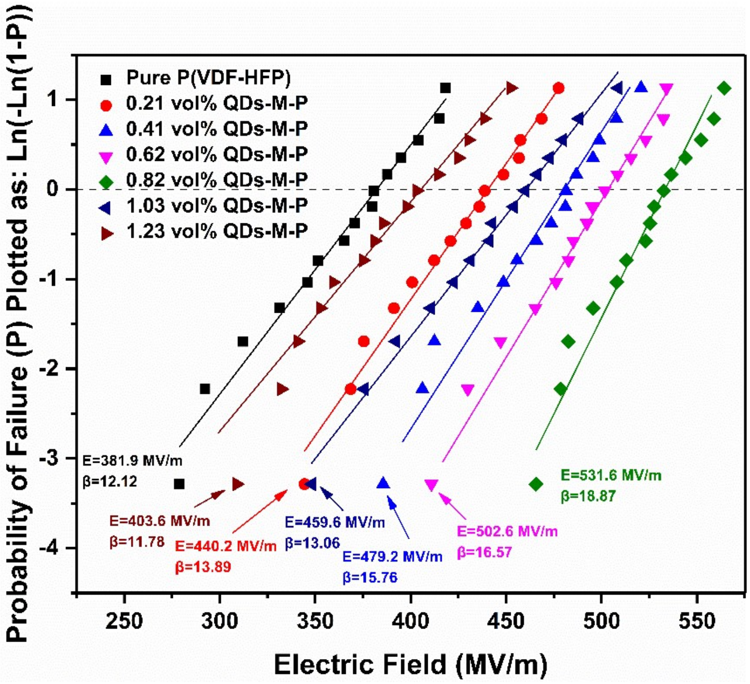

Fig. 18. Weibull plots of pure P(VDF-HFP) and a series of P(VDF-HFP)/QDs–M–P nanocomposites.

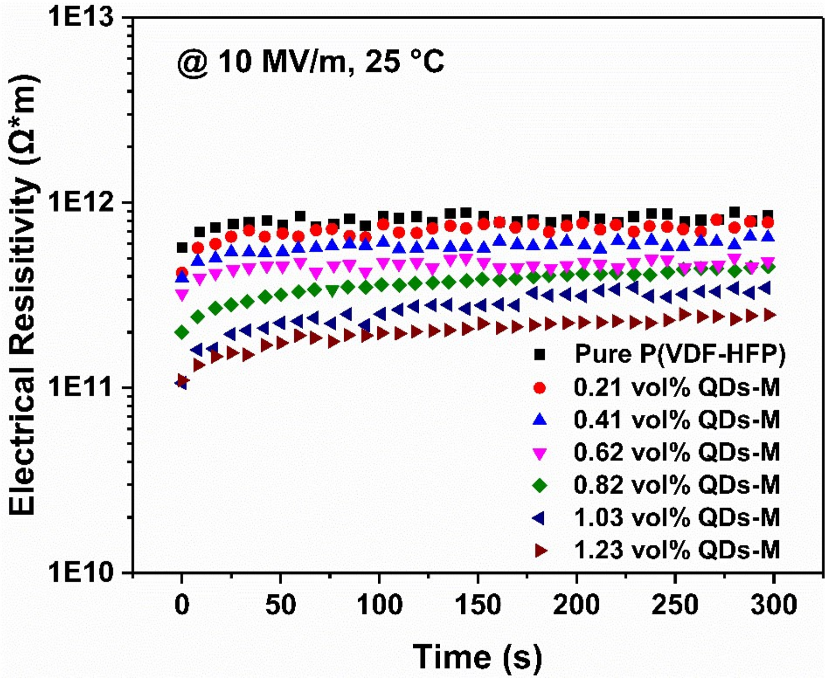

Fig. S19. Electric resistivity of pure P(VDF-HFP) and a series of P(VDF-HFP)/QDs–M nanocomposites under 10 MV m^{-1}at 25 °C.

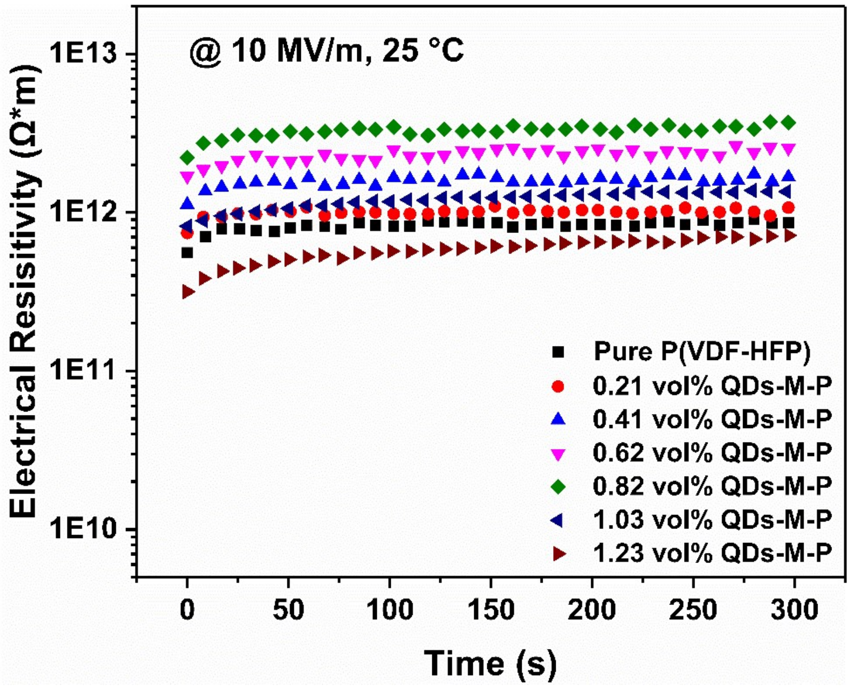

Fig. S20. Electric resistivity of pure P(VDF-HFP) and a series of P(VDF-HFP)/QDs–M–P nanocomposites under 10 MV m^{-1} at 25 °C.

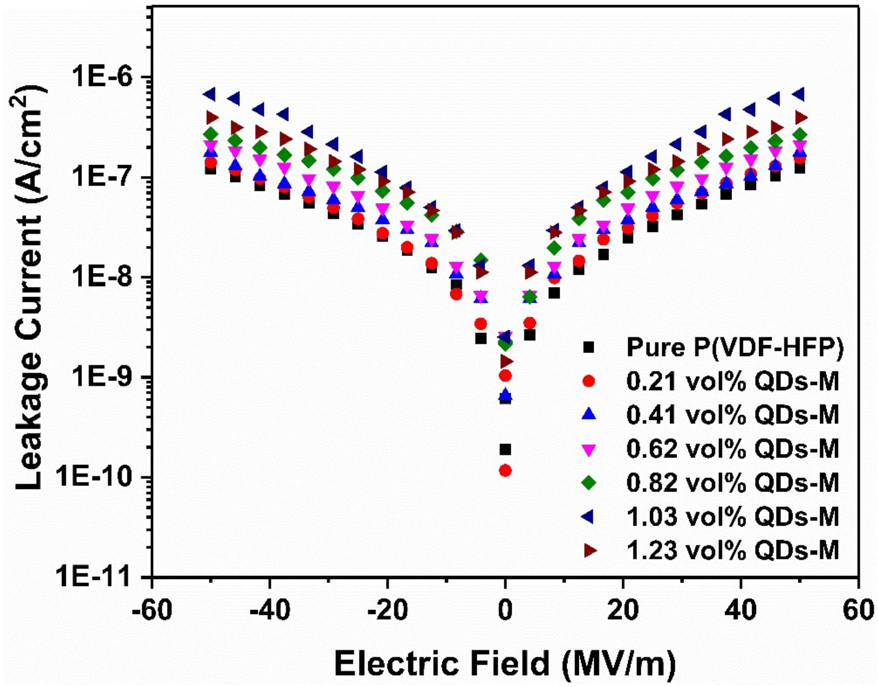

Fig. S21. Leakage current of pure P(VDF-HFP) and a series of P(VDF-HFP)/QDs–M nanocomposites as a function of electric field.

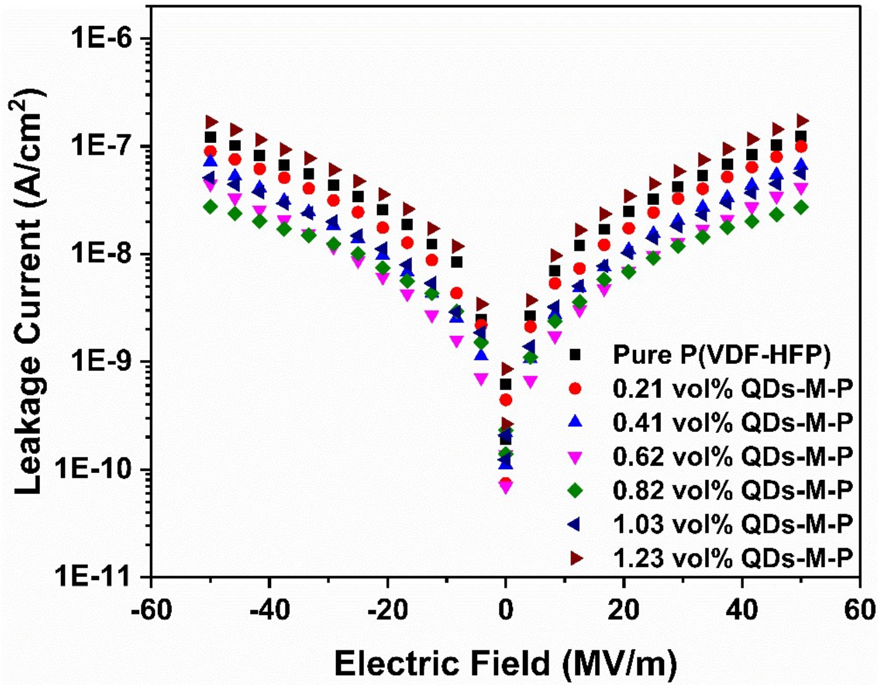

Fig. S22. Leakage current of pure P(VDF-HFP) and a series of P(VDF-HFP)/QDs–M–P nanocomposites as a function of electric field.

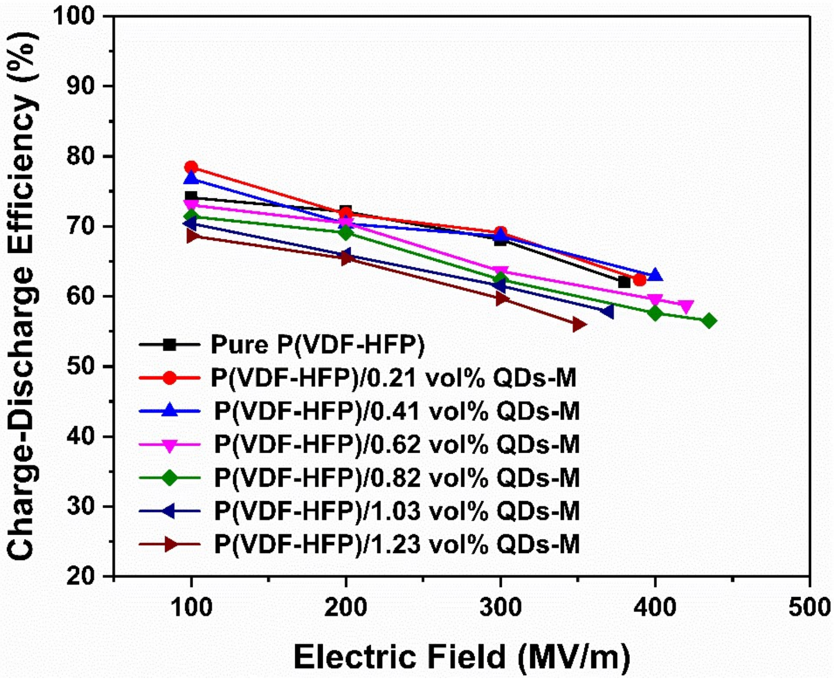

Fig. S23. Charge-discharge efficiency of pure P(VDF-HFP) and a series of P(VDF-HFP)/QDs–M nanocomposites.

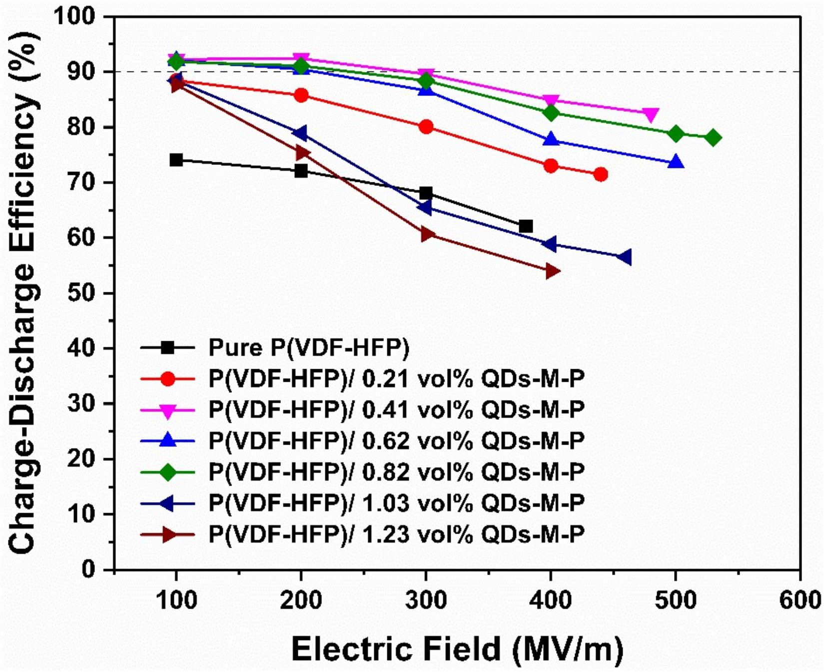

Fig. S24. Charge-discharge efficiency of pure P(VDF-HFP) and a series of P(VDF-HFP)/QDs–M–P nanocomposites.

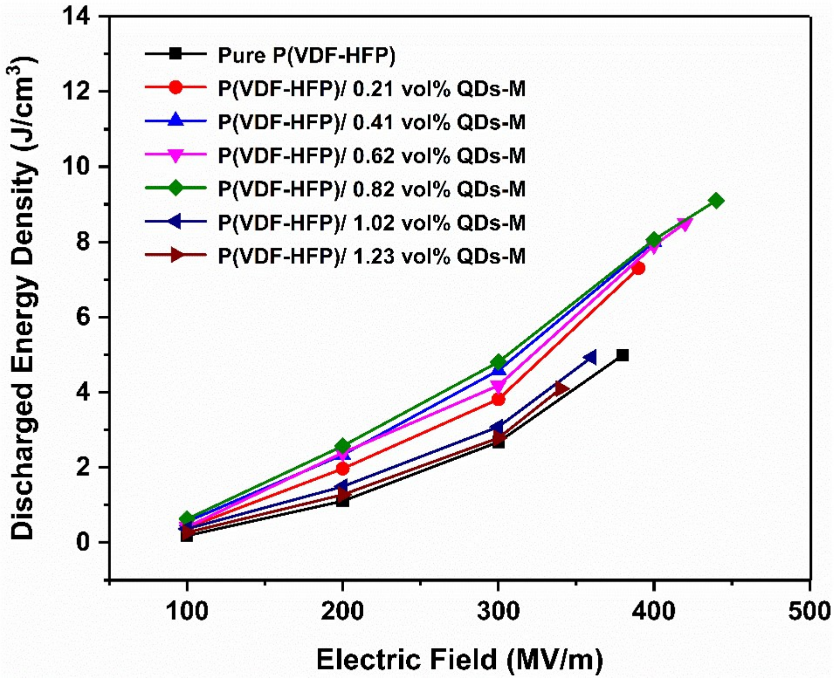

Fig. S25. Discharge energy density of pure P(VDF-HFP) and a series of P(VDF-HFP)/QDs–M nanocomposites as a function of electric field.

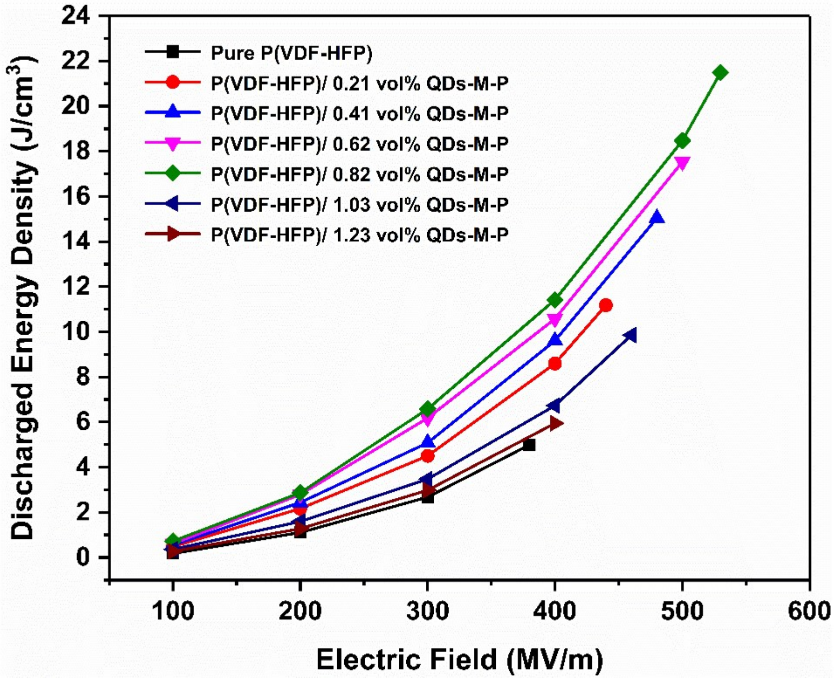

Fig. S26. Discharge energy density of pure P(VDF-HFP) and a series of P(VDF-HFP)/QDs–M–P nanocomposites as a function of electric field.

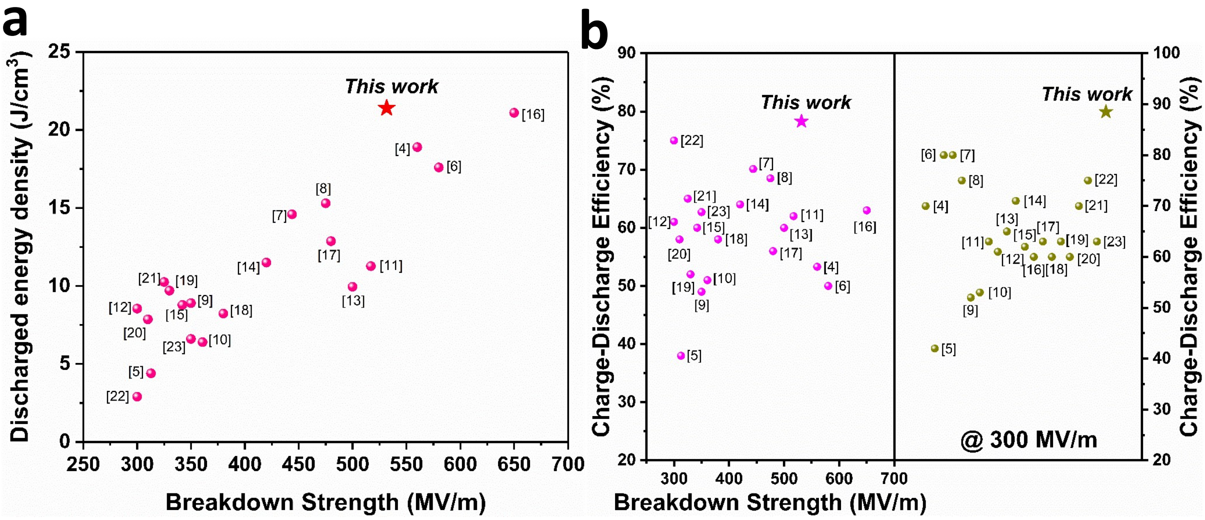

Fig. S27. Comparison of a) discharged energy density under breakdown strength and b) charge-discharge efficiency under breakdown strength (left) and 300 MV m^{-1} (right) between this work and literatures.

Table S1. Comparison of dielectric constant (K), dielectric loss (tanδ), breakdown strength (E_b), discharged energy density (U_e) and efficiency (η) between this work and literatures.

Polymer	Filler	Filler ratio	Ka)	tanδb)	E_b [MV m⁻	U_e [J cm^{-3}]c)	η [%]d)	η [%]e)	Ref.
PVDF	BZCT@SOf)	3 vol%	26.1	0.05	560	18.9	~53.3	~70	Zhang[4]
PVDF	TO–BT–TOg)	11 vol%	12.6	~0.08	312.8	4.4	~38	~42	Bhunia[5]
PVDF	BT@BNh)	5 wt%	11.3	~0.03	580	~17.6	~50	~80	Luo[6]
P(VDF-HFP)	NN@AOi)	3 vol%	~12	~0.03	443.8	14.59	70.1	~80	Pan[7]
PVDF	ST@AOj)	5 vol%	~10.5	~0.026	475	15.3	68.5	~75	Pan[8]
PVDF	Fe_3O_4@BN	5 vol%	16.5	0.025	350	8.9	~49	~52	Zhang[9]
PVDF	Pt@BT	1 wt%	~14	~0.07	360.7	6.4	51	~53	Wang[10]
PVDF	BT	4 vol%	10.8	~0.05	517	11.27	~62	~63	Hu[11]
P(VDF-HFP)	BT	3 vol%	~18	~0.06	300	8.55	61	61	Li[12]
P(VDF-HFP)	BT@SO	5 wt%	~11	~0.06	500	9.95	60	65	Kang[13]
PVDF	BT@SO	3 vol%	~11	~0.03	420	11.5	64	71	Bi[14]
PVDF	TO@BT	2.5 vol%	~13	~0.04	342	8.78	60	~62	Hu[15]
PVDF	TO	1 wt%	~12	~0.03	650	21.1	~63	~60	Wen[16]
P(VDF-HFP)	BT@*f*–PDAk)	5 vol%	~13	~0.05	480	12.87	56	~63	Wang[17]
PVDF	BZCT	2.1 vol%	12	0.028	380	8.23	~58	~60	Pan[18]
P(VDF-HFP)	BT	30 vol%	~18	~0.05	330	9.7	~52	~63	Hao[19]
PVDF	BZCT	3 vol%	~13	~0.03	310	7.86	58	~60	Chi[20]
PVDF	BT–Ag	2.5 vol%	15	~0.02	325	10.25	65	~70	Liu[21]
PVDF	BT@PDA	7 wt%	~25	~0.15	300	2.9	75	75	Xie[22]

PVDF	BT@SO	2.5 vol%	–	–	350	6.6	62.7	~63	Liu[23]
P(VDF-HFP)	**QDs–M–P**	**0.82 vol%**	**17.8**	**0.029**	**531.6**	**21.4**	**78.3**	**87.5**	**This work**

[a]dielectric constant at 1 kHz; [b]dielectric loss at 1 kHz; [c]discharged energy density under maximum electric field; [d]discharged efficiency under maximum electric field; [e]discharged efficiency under 300 MV m^{-1}; [f]$0.5(Ba_{0.7}Ca_{0.3})TiO_3$–$Ba(Zr_{0.2}Ti_{0.8})O_3$; [g]$TiO_2$−$BaTiO_3$−$TiO_2$; [h]$BaTiO_3$@BN nanosheets; [i]$NaNbO_3$@$Al_2O_3$; [j]$SrTiO_3$@$Al_2O_3$ and [k]$BaTiO_3$@fluoro-polydopamine.

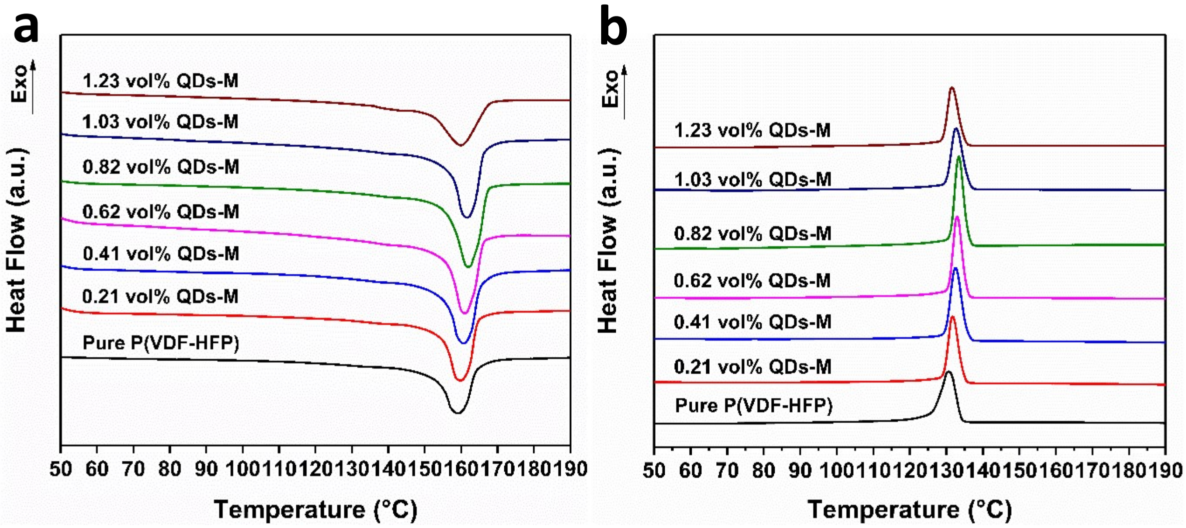

Fig. S28. DSC curves of pure P(VDF-HFP) and a series of P(VDF-HFP)/QDs–M nanocomposites under a) heating and b) cooling cycles.

Table S2. Crystallization temperatures (T_c), melting points (T_m) and crystallinities of pure P(VDF-HFP) and a series of P(VDF-HFP)/QDs–M nanocomposite films with different QDs–M content.

Sample	T_c [°C]	T_m [°C]	Crystallinity [%][a)]
P(VDF-HFP)	130.5	159.2	25.3
P(VDF-HFP)/0.21 vol% QDs–M	131.8	159.8	26.8
P(VDF-HFP)/0.41 vol% QDs–M	132.5	160.7	29.0
P(VDF-HFP)/0.62 vol% QDs–M	132.8	161.1	33.2
P(VDF-HFP)/0.82 vol% QDs–M	133.4	162.0	36.2
P(VDF-HFP)/1.03 vol% QDs–M	132.6	161.5	31.5
P(VDF-HFP)/1.23 vol% QDs–M	131.5	159.9	28.8

[a)] The crystallinity (X_c) is calculated *via* the following equation:

$$X_c = \frac{\Delta H_m}{\Delta H_0} \times 100\% \qquad (8)$$

where ΔH_m is the enthalpy of fusion derived from DSC melting curves and the weight of film samples, and ΔH_0 is the heat of fusion of 100% crystalline P(VDF-HFP), which is reported to be 104.7 J/g.[24]

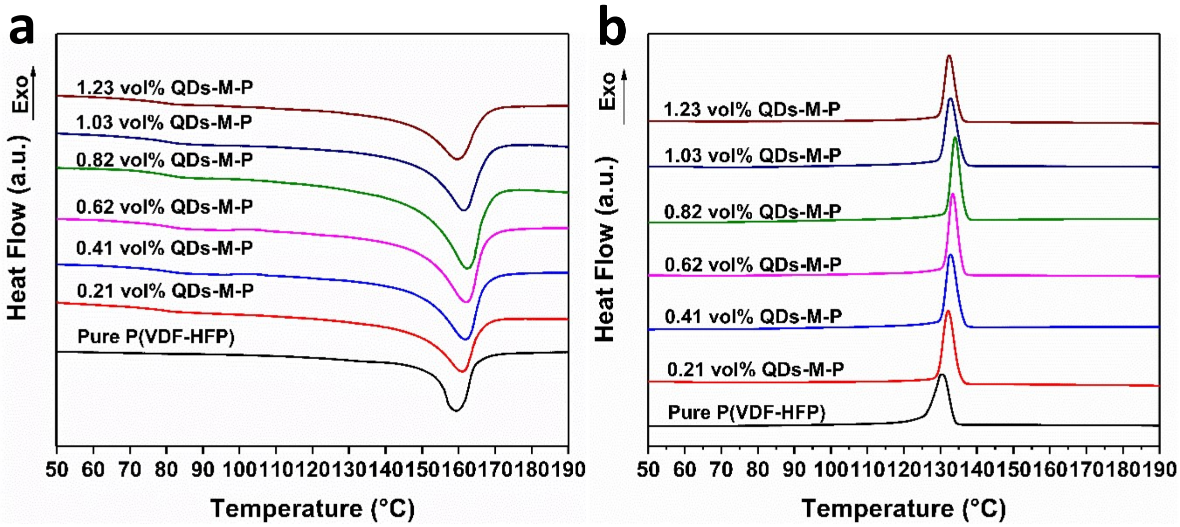

Fig. S29. DSC curves of pure P(VDF-HFP) and a series of P(VDF-HFP)/QDs–M–P nanocomposites under a) heating and b) cooling cycles.

Table S3. Crystallization temperatures (T_c), melting points (T_m) and crystallinities of pure P(VDF-HFP) and a series of P(VDF-HFP)/QDs–M–P nanocomposite films with different QDs–M content.

Sample	T_c [°C]	T_m [°C]	Crystallinity [%]
P(VDF-HFP)	130.5	159.2	25.3
P(VDF-HFP)/0.21 vol% QDs–M–P	132.1	160.9	27.9
P(VDF-HFP)/0.41 vol% QDs–M–P	132.8	161.5	29.7
P(VDF-HFP)/0.62 vol% QDs–M–P	133.3	162.2	35.4
P(VDF-HFP)/0.82 vol% QDs–M–P	134.0	162.4	38.3
P(VDF-HFP)/1.03 vol% QDs–M–P	132.7	161.5	34.5
P(VDF-HFP)/1.23 vol% QDs–M–P	132.4	159.7	29.9

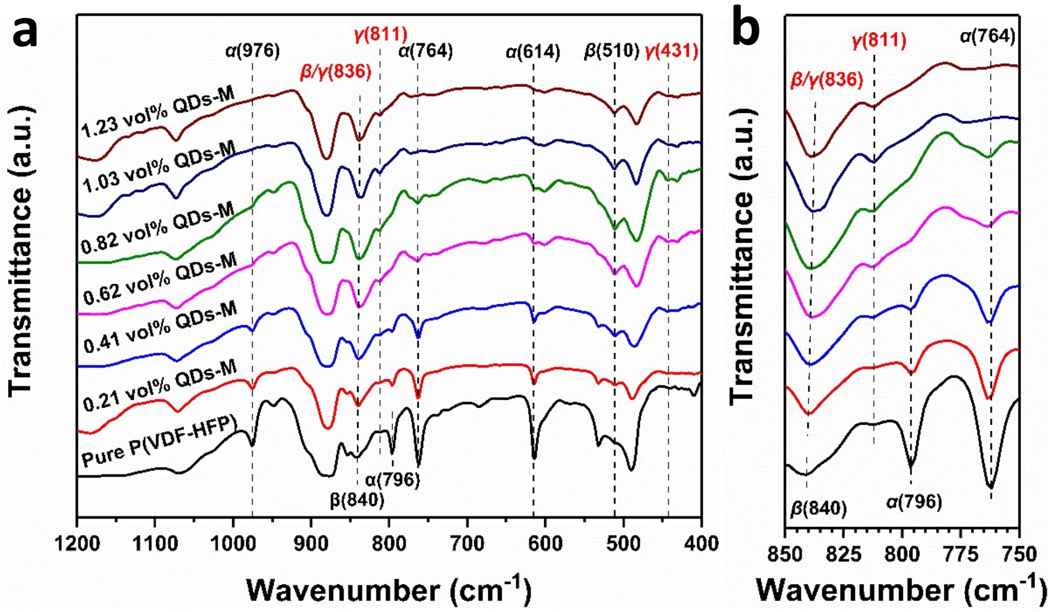

Fig. S30. a) FTIR spectra of pure P(VDF-HFP) and a series of P(VDF-HFP)/QDs–M nanocomposites. b) Enlarged view of the FTIR spectra with a wavenumber range from 850 cm^{-1} to 750 cm^{-1}.

Table S4. Relative fractions of TGTG', TTTT and T_3GT_3G' conformations (corresponding to α, β and γ phases of P(VDF-HFP), respectively) of pure P(VDF-HFP) and a series of P(VDF-HFP)/QDs-M nanocomposites.

Sample	TGTG' (α) [%]	TTTT (β) [%]	T_3GT_3G' (γ) [%]
P(VDF-HFP)	74.5	21.2	4.3
P(VDF-HFP)/0.21 vol% QDs–M	55.2	38.3	6.5
P(VDF-HFP)/0.41 vol% QDs–M	42.8	46.7	10.5
P(VDF-HFP)/0.62 vol% QDs–M	30.4	53.9	15.7
P(VDF-HFP)/0.82 vol% QDs–M	18.6	60.4	21.4
P(VDF-HFP)/1.03 vol% QDs–M	3.5	73.4	23.1
P(VDF-HFP)/1.23 vol% QDs–M	1.4	74.5	24.1

Calculation is conducted based on characteristic absorbance bands of the three phases and can be divided into two steps due to observed coexistence of three phases: first determine the polar/non-polar phase ratios and then calculate the β and γ phase ratios. The first step is performed according to the following equation:[25]

$$F_p = \frac{A_p}{\left(\frac{K_p}{K_n}\right)A_n + A_p} \times 100\% \qquad (9)$$

where F_p is the relative fraction of polar phases, A_p and A_n are the absorbencies at 836 and 764 cm^{-1}, respectively, and K_p, K_n represent the absorption coefficients: 7.7×10^4 and 6.1×10^4 cm^2 mol^{-1} at the respective wavenumbers. The ratios of β and γ phases are further calculated through a similar method using the absorbance of their characteristic bands at 510 and 811 cm^{-1}, respectively.

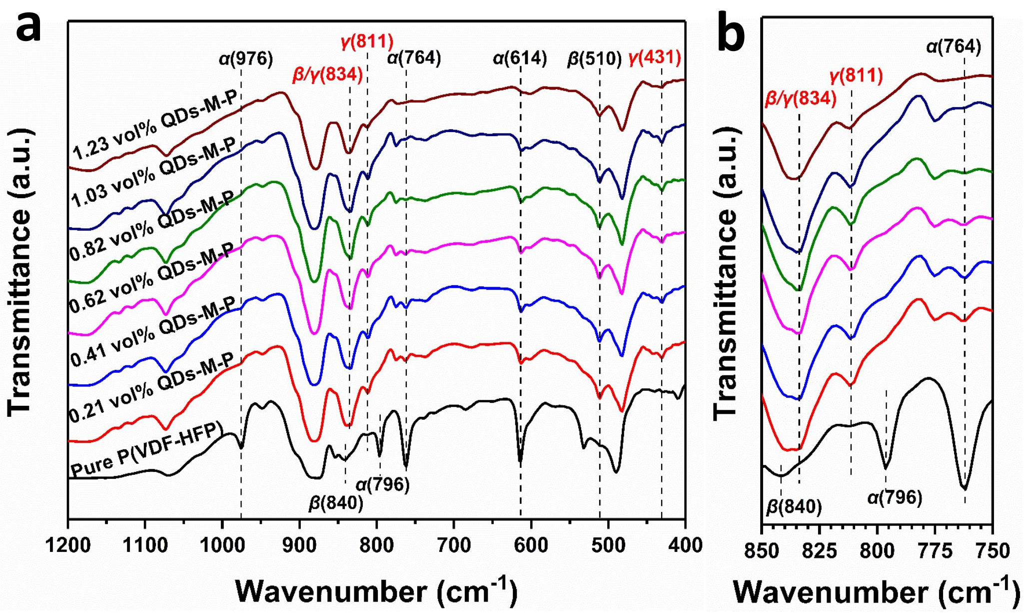

Fig. S31. a) FTIR spectra of pure P(VDF-HFP) and a series of P(VDF-HFP)/QDs–M–P nanocomposites. b) Enlarged view of the FTIR spectra with a wavenumber range from 850 cm^{-1} to 750 cm^{-1}.

Table S5. Relative fractions of TGTG', TTTT and T$_3$GT$_3$G' conformations (corresponding to α, β and γ phases of P(VDF-HFP), respectively) of pure P(VDF-HFP) and a series of P(VDF-HFP)/QDs-M nanocomposites.

Sample	TGTG' (α) [%]	TTTT (β) [%]	T$_3$GT$_3$G' (γ) [%]
P(VDF-HFP)	74.5	21.2	4.3
P(VDF-HFP)/0.21 vol% QDs–M-P	26.4	48.0	25.6
P(VDF-HFP)/0.41 vol% QDs–M-P	20.7	49.9	29.4
P(VDF-HFP)/0.62 vol% QDs–M-P	15.6	52.4	32.0
P(VDF-HFP)/0.82 vol% QDs–M-P	8.1	57.7	34.2
P(VDF-HFP)/1.03 vol% QDs–M-P	6.2	57.8	36.0
P(VDF-HFP)/1.23 vol% QDs–M-P	4.1	60.4	35.5

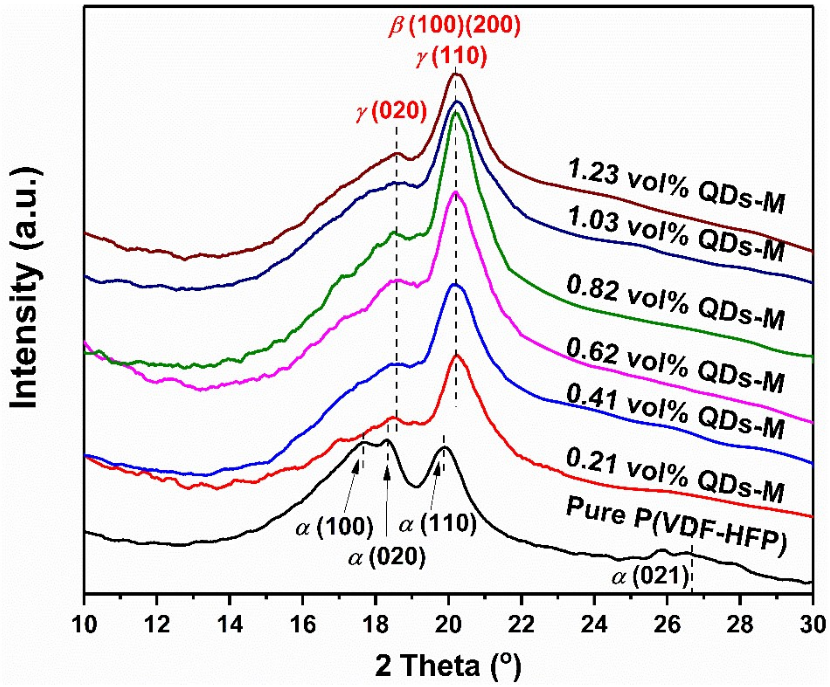

Fig. S32. XRD pattern of pure P(VDF-HFP) and a series of P(VDF-HFP)/QDs–M nanocomposites.

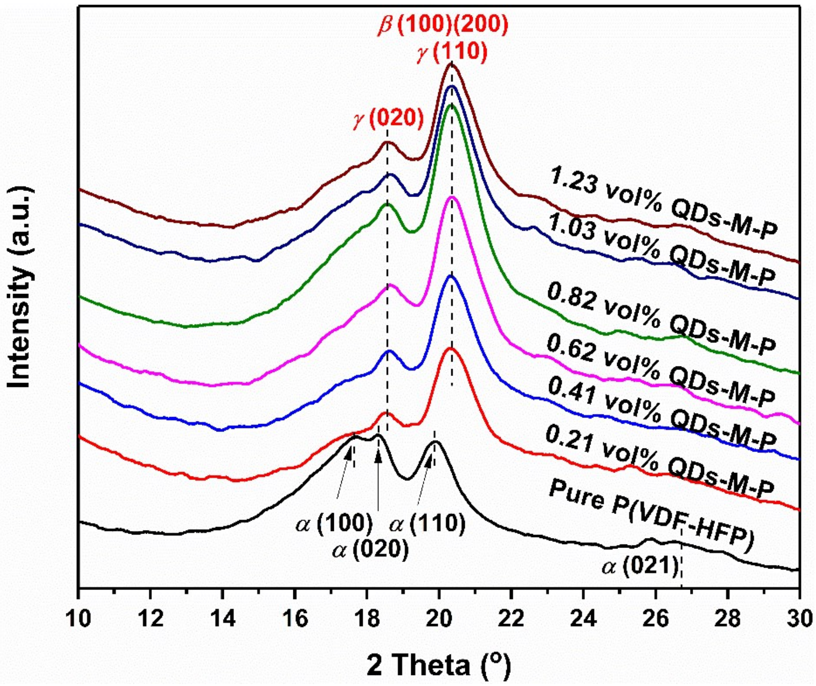

Fig. S33. XRD pattern of pure P(VDF-HFP) and a series of P(VDF-HFP)/QDs–M–P nanocomposites.

References

1 W. H. Bragg, W. L. Bragg, *Proc. R. Soc. Lond. Ser. Contain. Pap. Math. Phys. Character* 1913, **88**, 428.

2 B. D. Cullity, Reading, USA 1978, 32.

3 L. Vegard, *Z. Phys.* 1921, **5**, 17.

4 Y. Zhang, C. Zhang, Y. Feng, T. Zhang, Q. Chen, Q. Chi, L. Liu, G. Li, Y. Cui, X. Wang, Z. Dang, Q. Lei, *Nano Energy* 2019, **56**, 138.

5 Prateek, R. Bhunia, S. Siddiqui, A. Garg, R. K. Gupta, *ACS Appl. Mater. Interfaces* 2019, **11**, 14329.

6 S. Luo, J. Yu, S. Yu, R. Sun, L. Cao, W.-H. Liao, C.-P. Wong, *Adv. Energy Mater.* 2019, **9**, 1803204.

7 Z. Pan, Q. Ding, L. Yao, S. Huang, S. Xin, J. Liu, J. Chen, J. Zhai, *Nanoscale* 2019, **11**, 10546.

8 Z. Pan, L. Yao, J. Liu, X. Liu, F. Pi, J. Chen, B. Shen, J. Zhai, *J. Mater. Chem. C* 2019, **7**, 405.

9 Y. Zhang, T. Zhang, L. Liu, Q. Chi, C. Zhang, Q. Chen, Y. Cui, X. Wang, Q. Lei, *J. Phys. Chem. C* 2018, **122**, 1500.

10 L. Wang, X. Huang, Y. Zhu, P. Jiang, *Phys. Chem. Chem. Phys.* 2018, **20**, 5001.

11 P. Hu, S. Gao, Y. Zhang, L. Zhang, C. Wang, *Compos. Sci. Technol.* 2018, **156**, 109.

12 Z. Li, F. Liu, G. Yang, H. Li, L. Dong, C. Xiong, Q. Wang, *Compos. Sci. Technol.* 2018, **164**, 214.

13 D. Kang, G. Wang, Y. Huang, P. Jiang, X. Huang, *ACS Appl. Mater. Interfaces* 2018, **10**, 4077.

14 K. Bi, M. Bi, Y. Hao, W. Luo, Z. Cai, X. Wang, Y. Huang, *Nano Energy* 2018, **51**, 513.

15 P. Hu, Z. Jia, Z. Shen, P. Wang, X. Liu, *Appl. Surf. Sci.* 2018, **441**, 824.

16 R. Wen, J. Guo, C. Zhao, Y. Liu, *Adv. Mater. Interfaces* 2018, **5**, 1701088.

17 G. Wang, X. Huang, P. Jiang, *ACS Appl. Mater. Interfaces* 2017, **9**, 7547.
18 Z. Pan, L. Yao, J. Zhai, H. Wang, B. Shen, *ACS Appl. Mater. Interfaces* 2017, **9**, 14337.
19 Y. Hao, X. Wang, K. Bi, J. Zhang, Y. Huang, L. Wu, P. Zhao, K. Xu, M. Lei, L. Li, *Nano Energy* 2017, **31**, 49.
20 Q. Chi, T. Ma, Y. Zhang, Y. Cui, C. Zhang, J. Lin, X. Wang, Q. Lei, *J. Mater. Chem. A* 2017, **5**, 16757.
21 H. Liu, S. Luo, S. Yu, S. Ding, Y. Shen, R. Sun, C. Wong, *IEEE T. Dielect. El. In.* 2017, **24**, 757.
22 Y. Xie, Y. Yu, Y. Feng, W. Jiang, Z. Zhang, *ACS Appl. Mater. Interfaces* 2017, **9**, 2995.
23 S. Liu, J. Wang, J. Wang, B. Shen, J. Zhai, C. Guo, J. Zhou, *Mater. Lett.* 2017, **189**, 176.
24 M. C. García-Payo, M. Essalhi and M. Khayet, *J. Membrane Sci.*, 2010, **347**, 209.
25 J. Gregorio, Rinaldo, M. Cestari, *J. Polym. Sci., Part B: Polym. Phys.* 1994, **32**, 859.